JOURNAL OF AIRCRAFT
Vol. 47, No. 3, May–June 2010

# Design Forum

*DESIGN FORUM papers range from design case studies to presentations of new methodologies to speculations about emerging design trends. They vary from 2500 to 12,000 words (where a figure or table counts as 200 words). Following informal review by the Editors, they may be published within a few months of the date of receipt. Style requirements are the same as for regular contributions (see inside back cover).*

# Segmented-Free-Wing Concept for Gust Alleviation

Jason Welstead* and Gilbert L. Crouse Jr.†
*Auburn University, Auburn, Alabama 36849*

DOI: 10.2514/1.46481

**A promising technology for gust alleviation is the free wing. A free-wing design allows the wing to adjust itself in pitch about a spanwise axis in response to aerodynamic loads rather than being rigidly attached to the aircraft fuselage. The extension of the concept proposed here is called a segmented free wing and differs from a conventional free wing by sectioning the wing into multiple independent segments. This allows the wing to adjust to not only time-varying gust fields but also to gust fields that vary across the span. Initial wind-tunnel results showed an almost 40% reduction in rolling moment for a segmented free wing when subjected to an asymmetric velocity field, when compared with a traditional free-wing design. A 13.3-ft-span model was constructed, and experimental tests of this model showed a divergent oscillatory roll mode that appears with increasing velocity. An analytical model of the experimental test was developed that successfully predicts the instability. Comparison of the analytical model with the experimental results shows an overprediction of the stability of the system by the analytical model, and causes for the overestimation were investigated. Using the analytical model and experimental model, a successful solution to the roll instability was devised and tested.**

## Nomenclature

| | | |
|---|---|---|
| $a$ | = | hinge location as fraction of half-chord |
| $b$ | = | half-chord |
| $C$ | = | material damping |
| $C_{ij}$ | = | influence matrix elements |
| $C_L$ | = | coefficient of lift |
| $C_{L_\alpha}$ | = | lift-curve slope |
| $C_M$ | = | moment coefficient |
| $G$ | = | shear modulus of elasticity |
| $h$ | = | aerodynamic plunging |
| $I_{xx}$ | = | rolling mass moment of inertia |
| $I_{yy}$ | = | pitching mass moment of inertia |
| $J$ | = | polar area moment of inertia |
| $K$ | = | spring force |
| $L$ | = | lift |
| $L_B$ | = | beam length |
| $L'$ | = | lift per unit span |
| $M$ | = | moment |
| $M_{\text{aero}}$ | = | aerodynamic pitching moment |
| $M_x$ | = | rolling moment |
| $M_y$ | = | pitching moment |
| $M'$ | = | moment per unit span |
| $m$ | = | mass of wing segment |
| $m_{\text{cw}}$ | = | mass of counterweight |
| $s$ | = | distance traveled in half-chords, $Ut/b$ |
| $t$ | = | time |
| $U$ | = | velocity |
| $X_{\text{ac}}$ | = | aerodynamic center in percent chord |
| $X_1$ | = | unsteady aerodynamic term |
| $X_2$ | = | unsteady aerodynamic term |
| $x$ | = | segment width |
| $y$ | = | distance from segment center to origin |
| $\alpha$ | = | angle of attack |
| $\Gamma$ | = | circulation |
| $\delta_x$ | = | center-of-gravity offset distance |
| $\theta$ | = | pitch angle |
| $\rho$ | = | air density |
| $\rho_{\text{seg}}$ | = | material density of wing segment |
| $\phi$ | = | roll angle |

Presented as Paper 1901 at the AIAA Infotech@Aerospace Conference and AIAA Unmanned..Unlimited Conference, Seattle, WA, 6–9 April 2009; received 24 July 2009; revision received 25 September 2009; accepted for publication 1 October 2009. 

*Graduate Student, Department of Aerospace Engineering, 211 Davis Hall. Student Member AIAA.

†Associate Professor, Department of Aerospace Engineering, 211 Davis Hall. Senior Member AIAA.

## Introduction

TURBULENCE in the troposphere has long been an issue for aircraft of all sizes. However, aircraft with lower wing loadings are much more sensitive to turbulence than are aircraft with high wing loadings. The high sensitivity to turbulence as seen in general aviation aircraft and unmanned aerial systems (UAS) causes passenger discomfort, sensor malfunction, or potentially fatal loss of control. High-altitude long-endurance (HALE) aircraft are even more sensitive to turbulence than are the standard UAS or small aircraft because of their very low wing loading and light construction. An example of this type of problem was experienced by NASA's Helios project, a HALE aircraft with a wing span of 247 ft. The Helios aircraft took off from Kauai, Hawaii, on 26 June 2003 and flew approximately 30 min until a divergent pitch oscillation occurred "in which the airspeed excursions from the nominal flight

speed about doubled every cycle of the oscillation" [1]. The design speed of the aircraft was subsequently exceeded, causing dynamic pressures to increase beyond the designed limits of the structure. Under the intense load, the vehicle began to break up and it eventually crashed into the ocean. The final determination of the crash investigation was that the fatal pitch oscillation was caused by atmosphere disturbances, i.e., turbulence, which resulted in a structural failure of the system [1].

Various approaches to reduce sensitivity to turbulence are possible. One extreme approach would be to increase the wing loading of the HALE aircraft to be comparable with that of airliners; however, this is impractical in small aircraft, especially HALE aircraft. Increasing wing loading would strongly affect the mission performance of the airplane by reducing maximum endurance and reducing service ceiling. Increasing wing loading would also increase stall speed, which would negatively affect safety of operation. Another solution would be to increase the structural strength of the HALE aircraft to handle the dynamic loading under oscillatory conditions. However, this would increase the system weight, which would decrease performance, taking away from the HALE mission. Finally, a number of passive and active gust alleviation approaches have been proposed and implemented. Recent airliners such as the Boeing 787 and various Airbus models include active control systems to improve the ride quality through gusts and turbulence [2]. Active systems have been used for many years [3,4], but they do increase the complexity of the aircraft, requiring sensors to determine the gust field and a relatively sophisticated control system and actuators for best effect. A recent study coupled an active gust alleviation system with cruise flaps to both reduce drag and reduce gust response [5]. Passive systems have been used since the earliest days of flying when the Wright brothers tailored their wing design to improve its gust response [6]. Some passive systems have incorporated small wings to sense the gust field and provide negative feedback to the control system to offset the effect of gusts [7], while others have done aeroelastic tailoring to reduce gust response [8,9].

The passive approach for gust alleviation explored here is a variant of the free-wing design as depicted in Fig. 1. A free wing differs from a fixed wing in that the wing is free to pivot about a spanwise axis. The incidence of the free wing is thus independent of the incidence of the fuselage. The angle of incidence of the free wing is controlled by the aerodynamic forces acting on the wing and on a control surface at the trailing edge of the wing. Deflecting the control surface changes the equilibrium angle of attack and thus the lift coefficient produced by the wing. The advantage of the free wing is that the moment of inertia of the free wing is substantially lower than the moment of inertia of the entire aircraft. Thus, the free wing is able to react and adjust to changes in the gust field much more rapidly than the aircraft would in the case of a fixed-wing aircraft. NASA conducted several studies on the free-wing planform throughout the 1970s and early 1980s dealing with aircraft ranging from 3000 to 50,000 lb [10–14]. It was determined by Porter and Brown [10] that the free wing drastically reduced the load-factor response in all configurations by as much as 4 to 1. The major conclusion from the study was that the free wing was extremely effective at reducing the longitudinal response to disturbances for aircraft of common wingspans.

A limitation of the free-wing planform is that it can only adjust to time-varying turbulence. A feature of HALE aircraft is their large wingspans, which makes them susceptible to both time-varying and span-varying turbulence. The extension to the free-wing concept proposed here is called a segmented free wing and breaks the wing into multiple independent free-wing segments. Each segment is allowed to move and to be controlled independently from all of the other segments. The segmented-free-wing design shows promise for application to HALE aircraft, due to its ability to adjust to both time-varying and span-varying turbulence. Being a passive system, just like the free wing, no complex control systems need to be designed and implemented into the system, thus saving system complexity and weight. Each segment is free to pivot about its spanwise axis, allowing the entire wing to maintain a constant lift distribution even as the velocity field is changing. Additionally, the wing can alter its local pitch as disturbances vary across the span of the wing. Regardless of the turbulence profile across the planform, the segmented free wing can adjust to maintain a relatively constant lift distribution across the span and alleviate much of the roll response of the aircraft or spanwise bending moment placed on the wing structure. With this ability to deal with both time-varying and span-varying turbulence, the segmented free wing appears to be well suited for use in large-wingspan aircraft designs.

To evaluate the effectiveness of the segmented-free-wing concept, an initial wind-tunnel model was constructed. With promising results from these initial tests, a larger model was designed and fabricated. As will be described, tests on this larger model showed a dynamic instability. Consequently, the research then focused on developing an analytical model of the system to evaluate the stability of the system and better understand this instability. Finally, methods for stabilizing the system were explored both analytically with the dynamic model and experimentally with the test rig.

## Initial Wind-Tunnel Test

### Wind-Tunnel Model

A wind-tunnel model of the segmented free wing was designed and fabricated for use in the Auburn University $3 \times 4.25$ foot subsonic wind tunnel. The model had a wing span of 3 ft and was divided into six segments of equal size (approximately 6 in. span). Each segment had an 8 in. chord with the axis of rotation placed at 15% of the chord. The airfoil used was a NACA 0012 with a 20%-chord control surface at the trailing edge deflected $-5$ deg (trailing edge up). The wing segments were balanced about the pivot axis using lead shot, so the only net moments acting on the wing segments were the aerodynamic moments. The spar was made of $\frac{1}{2}$-in.-diam steel round stock to limit deflection. A $\frac{1}{16}$ in. spacer was placed between each segment to prevent the segments from interfering with each other. To create a spanwise flow variation in the wind tunnel, another wing was placed vertically in the wind tunnel upstream of the model to generate a trailed vortex just above the centerline of the model. This trailed vortex provided a significant spanwise variation in the flow over the model. The vortex generating wing was a cambered airfoil, approximately a NACA 2412 airfoil, with a span of 16 in. and a chord length of 8 in. The top of the wing was set at the midpoint of the test section, 18 in. above the floor. The trailing edge

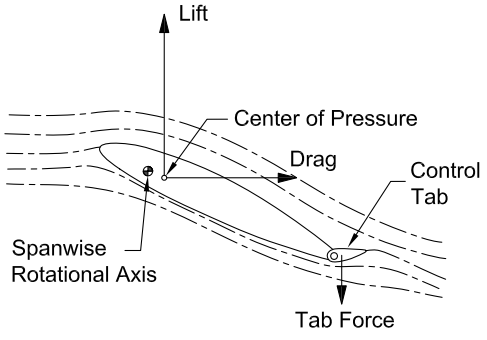


**Fig. 1 Cross-sectional illustration of the free-wing design [10].**

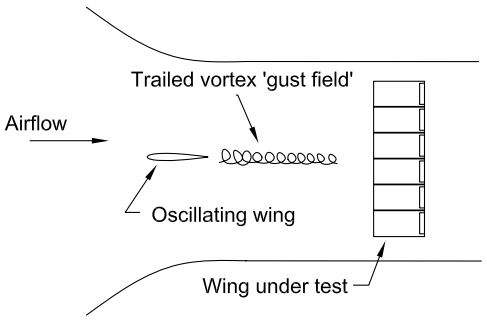


**Fig. 2 Wind-tunnel test schematic.**

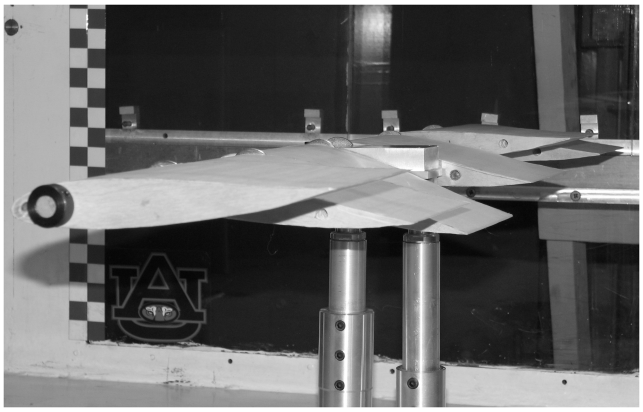

**Fig. 3 Segmented-free-wing model in the Auburn University wind tunnel.**

of the vortex generator wing was approximately 20 in. upstream of the leading edge of the wing under test. A schematic of the wind-tunnel setup can be seen in Fig. 2.

The wind-tunnel model was designed so that each individual segment could be connected to its neighbors. With the segments unconnected, the model behaved as a segmented free wing. By attaching all of the segments together, the model could simulate a traditional single free wing. By attaching the three segments on each half span together, it could simulate a free wing with independent left and right halves.

Figure 3 shows a photograph of the model in the wind tunnel with all of the segments free to rotate individually. The variation in angle of incidence across the six segments is easily seen as each individual segment adjusts to maintain constant aerodynamic angle of attack across the span in the presence of the trailed vortex above the wing.

Forces and moments on the wind-tunnel model were measured using a six-component, pyramidal, strain-gauge balance. Data were acquired over a 2 s period at a sample rate of 500 samples/second using 16-bit National Instruments analog-to-digital converters and Analog Devices instrumentation amplifiers. Before the test, calibration of the balance was conducted and verified using known weights. The maximum error measured during the verification was 2%. During a recent flow survey, flow angularity was measured at less than 2 deg in the horizontal plane [15].

#### Wind-Tunnel Results

Once the model was installed in the wind tunnel, each of the three wing configurations (i.e., single free wing, left/right independent free wing, and segmented free wing) was tested with the vortex generator wing in three different positions: full left deflection, neutral deflection, and full right deflection. The full left and right deflections corresponded to a deflection of approximately 15 deg. For each wing configuration and vortex generator position, the rolling moment generated by the spanwise flow variation over the model was measured. These data are presented in Table 1. For the purpose of calculating the force and moment coefficients, the reference area of the wing was 288 $\text{in.}^2$ and the reference span was 36 in. The spanwise center of pressure was calculated as a percentage of span by dividing the rolling moment coefficient by the normal force coefficient. The difference between the spanwise center of pressure at full left deflection and full right deflection of the vortex generator can be used as a metric to measure the amount of aerodynamic load that would be transmitted to the aircraft due to spanwise velocity variations. Using the center-of-pressure movement rather than rolling-moment-coefficient factors in the different lift coefficients produced by the different configurations.

For the single free wing, the center of pressure moves 4.16% (from −1.74% at negative deflection to 2.42% at positive deflection) of the span, due to the presence of the gust field. When each wing half is allowed to move freely from the other, this movement drops to 3.00%: a 28% reduction. The center-of-pressure movement is further reduced by the segmented free wing, which shows a center-of-pressure movement of 1.87%: a reduction of 38%. These results, although preliminary, show strong evidence that the segmented-free-wing design would significantly reduce structural loads due to spanwise variations in the flowfield.

Table 1 also shows the lift-to-drag ratios computed for the three configurations. The average values for the single free wing (6.26) and the left/right free wing (6.39) are very close. However, the segmented free wing shows an average lift-to-drag ratio of 5.21, which is a 17% reduction from the single-free-wing average. Looking more closely, this loss of $L/D$ arises from a 12% decrease in lift coefficient and a 6% increase in drag coefficient. Since the same model was used for each of the configurations, these differences can be attributed to induced effects. Each of the segments of the tested model had identical geometry; consequently, the segmented wing tried to maintain the same average aerodynamic angle of attack/lift coefficient across the entire span of the wing. This does not produce an efficient lift distribution. The lift distribution on any wing must drop to zero at the very tip of the wing [16]. For the average lift coefficient on the outboard segment to remain the same as the inboard segments while the lift coefficient at the tip drops to zero, the inboard side of the tip segment must be heavily loaded. This results in a very nonideal (nonelliptical) lift distribution that affects the efficiency of the wing. A fairly simple solution to this problem would be to adjust the flap deflection angles along the span to approximate an elliptical lift distribution. Since the flap deflection of each segment can be adjusted independently, the lift distribution can be tailored as desired. This is a further benefit of the segmented free wing. With the ability to tailor the lift distribution across the segments, a rectangular wing planform that is inexpensive to manufacture can be used while still achieving close to an elliptical lift distribution.

## Larger-Scale Model Test

#### Sizing and Configuration

With the success of the wind-tunnel testing, a larger model was designed and constructed for further testing. The larger segmented-free-wing model was designed to fit onto an existing modular testbed

**Table 1 Lift, drag, and rolling moments of three configurations**

| Vortex generator deflection | Lift coefficient | Drag coefficient | $L/D$ ratio | Rolling moment coefficient | Lateral center of pressure, % span |
|---|---|---|---|---|---|
| Single free wing | | | | | |
| Negative | 0.585 | 0.089 | 6.58 | −0.0102 | −1.74% |
| Neutral | 0.611 | 0.102 | 5.98 | −0.0057 | −0.94% |
| Positive | 0.631 | 0.102 | 6.22 | 0.0153 | 2.42% |
| Left/right free wing | | | | | |
| Negative | 0.590 | 0.088 | 6.69 | −0.0098 | −1.67% |
| Neutral | 0.610 | 0.099 | 6.18 | −0.0013 | −0.21% |
| Positive | 0.640 | 0.102 | 6.29 | 0.0085 | 1.33% |
| Segmented free wing | | | | | |
| Negative | 0.499 | 0.095 | 5.27 | −0.0078 | −1.57% |
| Neutral | 0.550 | 0.105 | 5.21 | −0.0026 | −0.48% |
| Positive | 0.559 | 0.109 | 5.14 | 0.0017 | 0.30% |

aircraft by replacing the existing fixed wings of that aircraft. The overall wingspan of the model was approximately 13.3 ft and had a chord of 16 in. The planform had no taper or sweep. Each half of the wing was divided into five equal segments approximately 14 in. wide, with a $\frac{1}{16}$ in. gap between each segment to prevent any interference between segments. A top view of the segmented free wing is shown in Fig. 4. Each individual segment was balanced about its hinge axis by adding counterweights extending in front of the segment. The total weight of the wing was 8.5 lb, including the counterweights.

### Airfoil Design

The airfoil shape selected was an airfoil designed for Freewing Aerial Robotics and used on their Scorpion unmanned aerial vehicle. This airfoil shape is shown in Fig. 5. The wing was constructed out of extruded polystyrene foam. Several sections of the inside of the wing were cut out to allow the passing of wires and to reduce weight. A counterweight was attached to the bottom side of each segment and extended forward of the leading edge with an approximately 1 oz weight attached. The counterweight moved the center of gravity forward to balance the segment on the spanwise pivot axis.

The airfoil was analyzed using Xfoil [17,18] to determine its aerodynamic center and lift-curve slope. A typical Reynolds number was calculated to be around 200,000 based on a 22 ft/s velocity and a 16 in. chord length. This Reynolds number was used for the viscous-boundary-layer analysis in Xfoil. As shown in Fig. 6, the lift-curve slope $C_{l_\alpha}$ was calculated to be 7.56/rad (0.132/deg). Figure 7 shows the pitching moment of the airfoil about its quarter-chord point as a function of lift coefficient. A linear trend line from regression analysis has been drawn on the graph along with the trend line equation. The aerodynamic center of the airfoil was found by adding one-fourth to the inverse slope of the trend line. At 29% of the chord, the aerodynamic center for this airfoil is considerably further aft than the typical thin airfoil theory value of 25% of the chord.

To maintain static pitch stability of a free-wing segment the pivot axis must be ahead of the aerodynamic center of the segment [10]. The aerodynamic center is usually near the quarter-chord [16], so the hinge margin is defined as the distance the pivot axis is ahead of the quarter-chord line in percentage of the chord. Hinge margins ranging from $0.05c$ to $0.20c$ were examined by Porter and Brown [10] as well as the effect of the hinge margin on the required control tab sizing. In this study, a hinge margin of $0.05c$ was chosen in order to reduce the amount of ballast required to balance the wing segments. With this hinge margin, the pivot axis (which was the main wing spar) was located at 20% of the chord. Vertically, the spar was centered on the chord line.

A control tab located at the trailing edge was the only control device on the segmented free wing. The control tab could deflect $\pm 20$ deg, had a chord length of 25% of the wing chord, and spanned the entire trailing edge of each segment. Each segment's control tab was actuated using an electric servo motor embedded in the airfoil and covered using a plastic skinning material.

### Experimental Setup

The larger-scale segmented-free-wing model was tested experimentally by mounting the model on a truck. The wing was mounted to a $3 \times 3.5$ in. wood beam (constructed from a pair of $2 \times 4$ boards)

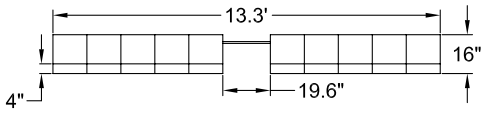


**Fig. 4 Segmented free wing viewed from the top.**

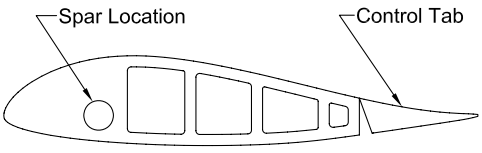


**Fig. 5 Free-wing airfoil design with control tab.**

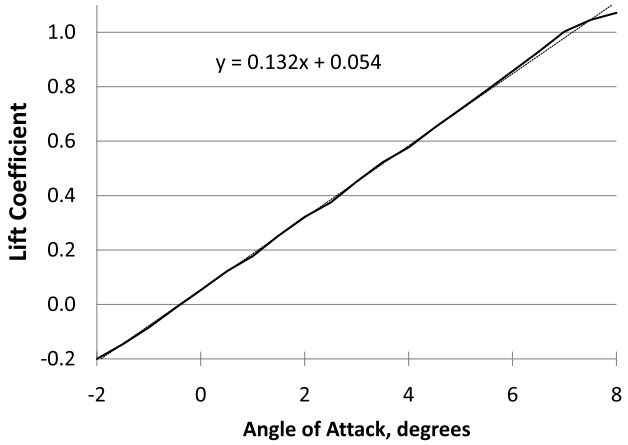


**Fig. 6 Lift coefficient versus angle of attack.**

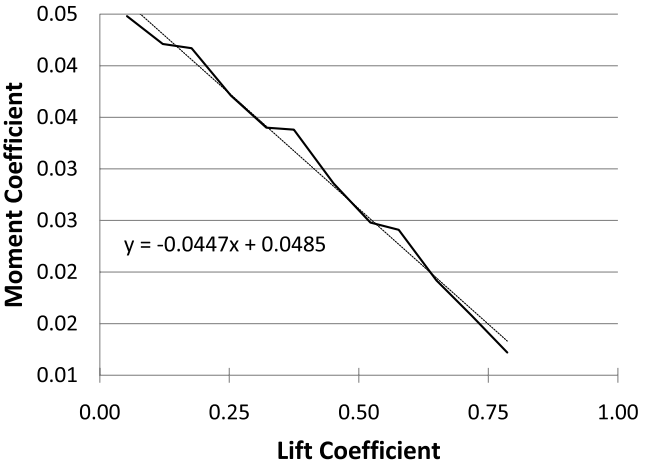


**Fig. 7 Pitching moment versus lift coefficient.**

that extended 7 ft in front of the truck, as shown in Figs. 8 and 9. Mounting the wing above and in front of the truck reduced the aerodynamic influence of the truck on the wing. The wing was rigidly mounted to the beam so that roll was mechanically restrained. The control tabs on each of the wing segments were controlled via a radio transmitter so that the angle of attack of the segments could be varied from within the truck cab during testing.

### Larger-Scale Model Results

The experiments with the larger-scale model were conducted on a large open airplane parking area at the Auburn Opelika Airport (Federal Aviation Administration designation KAUO). With the rig attached to the full-size pickup truck, the speed of the truck was slowly increased while observing the results. Digital videos of the tests were acquired and used to estimate oscillation frequencies and onset velocities. Truck ground speed was measured using the truck speedometer. The speedometer was verified using a handheld Garmin Quest Global Positioning System at speeds of 22, 29, and 44 ft/s and read within 0.75 ft/s at each speed. At the time the experiment was conducted, the wind velocity at the airport was recorded by the airport's automated weather observing system as 10 ft/s at 130 deg. The truck was driven across the parking area at a

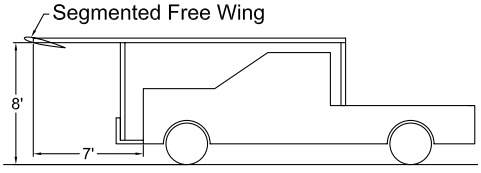


**Fig. 8 Diagram of the experimental setup.**

**Fig. 9 Segmented free wing mounted to a beam on the truck, looking through the windshield.**

40 deg course angle and reciprocal course of 220 deg. Consequently, the prevailing wind was perpendicular to the course driven. Airspeed was not measured directly but was inferred from the ground speed measurement.

At a ground speed of between 22–29 mph an unstable oscillatory rolling motion occurred during experimental testing. As velocity was increased, the frequency stayed the same but the amplitude increased dramatically. The system had an oscillation frequency of approximately 1.2 Hz with a maximum rolling angle of about 20 deg before the velocity was reduced.

To explore this behavior, several simple modifications to the model were explored, including changing the angle of the control tabs and taping multiple segments together. Neither of these had any significant affect on the instability, though taping segments together did increase the velocity at which the instability appeared. Additional modifications were then examined, including increasing the rolling moment of inertia of the system and changing the center of gravity of the wing segments. To increase the rolling moment of inertia, aluminum pipes were attached to the wingtips, extending beyond the wingtips by 2 ft on either side. This modification changed the frequency of oscillation but did not affect the stability. The center of gravity of the segments was modified by adding weight to the counterweight extending out in front of the leading edge of each segment. This also proved unsuccessful.

Porter and Brown [10] found a divergent spiral mode in their computational analysis of a free-wing aircraft with independent left and right wing panels. In the experimental apparatus described here, both yaw and roll were restrained so that a spiral motion was not possible. However, it is conjectured that the same mechanism driving the spiral mode in Porter and Brown's work is manifest here as an oscillatory roll mode due to the mechanical restraint.

**Fig. 10 Segmented free wing with 24 in. fixed segments attached to the tip.**

With the initial modifications to the experimental system proving unsuccessful, the design was modified to allow for the attachment of fixed segments on each wingtip. This design change allowed for various sizes of fixed segments to be attached. The chord length of the fixed segments was the same as the free-wing segments; however, the span of the segments varied from 6 to 24 in. The airfoil for the fixed segments was a symmetric NACA 0012 airfoil, and the fixed segments were placed at a zero angle of incidence to minimize the steady lift force generated by the fixed segments. Fixed segments of four different sizes (6, 12, 18, and 24 in. in span) were constructed and tested. The spar was place at the quarter-chord of the fixed segments to minimize the moment from the fixed segments.

The 24 in. segments were the first fixed segments tested during the experiment. With the fixed segments attached to the platform, the system no longer showed the divergent rolling oscillation that was seen in the previous experimental attempts. The platform remained straight and level throughout a large range of velocities, with a maximum sustained ground speed of 66 ft/s. A dihedral formed in the wings due to the lift being produced by the free-wing segments, as shown in Fig. 10. Very little movement occurred in the segments once equilibrium of the system was reached.

Testing continued with each of the other fixed segment sizes. The model demonstrated satisfactory stability using all sizes of fixed segments, including the 6 in. segment at ground speeds up to 66 ft/s. Any roll perturbations were quickly damped out and a steady equilibrium was quickly achieved for all fixed segment sizes.

## Analytical Model

Because of the dynamic instability observed during the experimental testing, a detailed mathematical model of the dynamics of the segmented free wing was developed in order to accurately predict and understand the behavior of the system. MATLAB 7.0 was used to run the calculations and to plot the results of the stability analyses. The mathematical model included a linear model of the system dynamics, and eigenanalysis was used to evaluate the behavior of the segmented-free-wing system.

The origin of the system was located at the intersection of the axis of symmetry and the centerline of the spar. The $x$ direction points forward from the leading edge of the wings, and the $y$ direction extends out the right wing, as shown in Fig. 11. The $z$ direction points downward to complete the triad. The system was modeled with 11 degrees of freedom: 10 different pitch angles, one for each segment, and a roll angle. The system was mechanically restrained to the support beam, resulting in no translational degrees of freedom. The translation of the truck was assumed to be a constant velocity in the $x$ direction.

### Governing Equations

Free-body diagrams of the segmented-free-wing system and a wing segment are shown in Figs. 12 and 13. From the free-body diagrams, equations modeling the segmented-free-wing system can be formulated.

The equation modeling rolling motion of the system is

$$M_x = I_{xx}\ddot{\phi} = -\sum_i L_i y_i - K\phi - C\dot{\phi} + \sum_i m y_i \delta_{x_i} \ddot{\theta}_i \qquad (1)$$

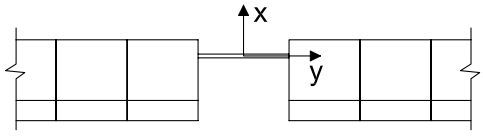


**Fig. 11 Axis configuration for analytical model.**

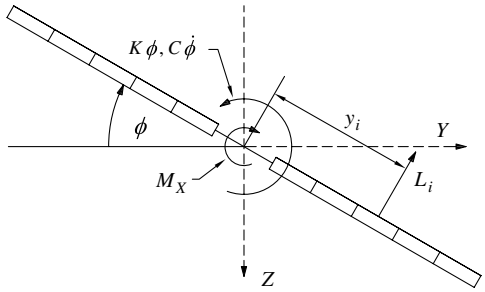


**Fig. 12 Free-body diagram of the segmented-free-wing system in roll, looking from the rear.**

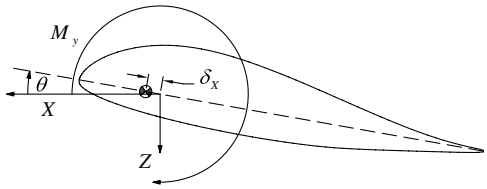


**Fig. 13 Free-body diagram of a wing segment.**

The final term in Eq. (1) takes into account the possible offset of the center of gravity of the wing segments from their pitch axes.

The equation for the pitching motion of each segment is

$$M_{y_i} = I_{yy}\ddot{\theta}_i = M_{\text{AERO}_i} + my_i\delta_{x_i}\ddot{\phi} \tag{2}$$

Once again, the final term accounts for the center-of-gravity offset from the segments' pitch axes.

### Aerodynamics

The aerodynamic lift and moment, $L_i$ and $M_{\text{AERO}_i}$, in Eqs. (1) and (2) are the most complex terms in the analytical model. Unsteady aerodynamic calculations were used to accurately model the aerodynamic forces and moments on the segmented free wing. To determine whether unsteady aerodynamics are significant for this problem or whether a quasi-steady approximation could be justified, a brief analysis using Theodorsen's function was completed. During experimental testing of the larger model an oscillation at a frequency of 1.2 Hz was observed at an airspeed of 22 fps. This corresponds to a reduced frequency of $k = 0.23$, which (using Theodorsen's function) produces a magnitude of the lift response of 0.72 and a phase shift of 0.2584 rad or 14.80 deg [19]. This indicates that a quasi-steady assumption would overpredict the lift response by over 25% and, clearly, unsteady effects are significant.

In unsteady aerodynamics, the lift response to a step change in angle of attack, known as the indicial response, can be modeled as [20]

$$\frac{C_L(s)}{\Delta\alpha} = C_{L_\alpha}\phi(s) \tag{3}$$

where $s$ represents the distance traveled in half-chords and $\phi(s)$ is the Wagner lift deficiency function. One approximation to the Wagner function is by R. T. Jones [20] and is highly accurate for intermediate values of $s$:

$$\phi(s) = 1 - A_1\exp(-b_1 s) - A_2\exp(-b_2 s) \tag{4}$$

where $A_1 = 0.165$, $A_2 = 0.335$, $b_1 = 0.0455$, and $b_2 = 0.3$. Given the indicial response, Duhamel's convolution integral [20] can be used to get the overall lift response to an arbitrary forcing function $\alpha(t)$:

$$C_L(t) = C_{L_\alpha}\left[\alpha(0) + \int_0^t \frac{\mathrm{d}}{\mathrm{d}\tau}\alpha(\tau)\phi\left(\frac{U}{b}(t-\tau)\right)\mathrm{d}\tau\right] \tag{5}$$

For the analytical model, it is desirable to have the unsteady terms in a state-space form as presented in Eq. (6):

$$\begin{Bmatrix}\dot{X}_1\\ \dot{X}_2\end{Bmatrix} = \mathbf{A}\begin{Bmatrix}X_1\\ X_2\end{Bmatrix} + \begin{bmatrix}1\\ 1\end{bmatrix}\alpha(t) \qquad C_L = \mathbf{C}\begin{Bmatrix}X_1\\ X_2\end{Bmatrix} + \mathbf{D}\alpha(t) \tag{6}$$

To find this state-space representation, the Laplace transforms of Eqs. (5) and (6) were taken and equated to give the unsteady circulatory lift per unit span:

$$\begin{Bmatrix}\dot{X}_1\\ \dot{X}_2\end{Bmatrix} = \begin{bmatrix}-b_1\frac{U}{b} & 0\\ 0 & -b_2\frac{U}{b}\end{bmatrix}\begin{Bmatrix}X_1\\ X_2\end{Bmatrix} + \begin{bmatrix}1\\ 1\end{bmatrix}\alpha(t)$$
$$L'_c = \rho U^2 b C_{L_\alpha}\left(\frac{U}{b}[A_1 b_1 \quad A_2 b_2]\begin{Bmatrix}X_1\\ X_2\end{Bmatrix}\right) + \begin{bmatrix}1\\ 1\end{bmatrix}\alpha(t) \tag{7}$$

The circulatory lift on the airfoil is affected by both the angle of attack and the pitch rate (rate of change of angle of incidence). From thin-airfoil theory, it is known that these two can be combined by referencing the angle of attack at the three-quarter-chord point [20]. Combining the pitching motion and the rolling motion of the wing, the angle of attack at the three-quarter-chord point can found from

$$\alpha_{\frac{3}{4}c} = \theta + \frac{1}{U}\left(y\dot{\phi} + \dot{\theta}b\left(\frac{1}{2} - a\right)\right) \tag{8}$$

which replaces the angle of attack term of the circulatory lift in Eq. (7).

In addition to the circulatory lift on the wing, there are also aerodynamic forces on the wing due to the mass of air surrounding the wing that must be pushed out of the way when the wing pitches or plunges up or down. These forces are called apparent mass or noncirculatory forces and can be written for lift [21]:

$$L'_{\text{NC}} = \rho\pi b^2(\ddot{h} + U\dot{\theta} - ba\ddot{\theta}) \tag{9}$$

Including both the circulatory and noncirculatory terms, the total lift per unit span can be written as

$$L' = \rho U^2 b C_{L_\alpha}\left(\frac{U}{b}[A_1 b_1 \quad A_2 b_2]\begin{Bmatrix}X_1\\ X_2\end{Bmatrix} + \frac{1}{2}\alpha_{\frac{3}{4}c}(t)\right)$$
$$+ \pi\rho b^2(\ddot{h} + U\dot{\theta} - ba\ddot{\theta}) \tag{10}$$

The aerodynamic pitching moment includes both circulatory and noncirculatory terms, as does the lift force. The circulatory moment is due to a constant term plus the circulatory lift force acting at the aerodynamic center of the wing segments. This can be written as

$$M'_C = \tfrac{1}{2}\rho U^2 b^2 C_{M_0} + b(\tfrac{1}{2} + a)L'_C \tag{11}$$

The noncirculatory terms for pitching moment are [21]

$$M'_{\text{NC}} = \pi\rho b^2\left(ba\ddot{h} + U\frac{b}{4}\left(a - \frac{1}{2}\right)\dot{\theta} - \frac{b^2}{16}\right) \tag{12}$$

which yields a total pitching moment per unit span of

$$M' = \frac{1}{2}\rho U^2 b^2 C_{M_0} + b\left(\frac{1}{2} + a\right)L'_C$$
$$+ \pi\rho b^2\left(ba\ddot{h} + U\frac{b}{4}\left(a - \frac{1}{2}\right)\dot{\theta} - \frac{b^2}{16}\left(a^2 + \frac{1}{8}\right)\ddot{\theta}\right) \tag{13}$$

### Validation of Aerodynamic Model

The analytical aerodynamic model was validated by comparing the circulatory lift response to Theodorsen's function and the total lift response to experimental data by Rainey [22] of a purely pitching wing. All roll terms in the lift and unsteady equations were ignored to allow for a purely pitching system. To compare the circulatory lift to Theodorsen's function, the Laplace transforms of Eqs. (7) and (9) were taken and the unsteady terms $X_1$ and $X_2$ were substituted into the lift equation. Dividing the lift equation by $\alpha$ and substituting $ik$ for the Laplace variable, the transfer function from angle of attack to lift response in terms of reduced frequency is written as

$$\frac{C_L(i\omega)}{\alpha(i\omega)} = C_{L_\alpha}\left(\frac{1}{2} + A_1 b_1 \frac{1}{ik + b_1} + A_2 b_2 \frac{1}{ik + b_2}\right) + \pi(ik + ak^2) \tag{14}$$

As indicated by Fung [19], the circulatory lift portion of this function should be equivalent to Theodorsen's function when normalized by the lift-curve slope.

In Fig. 14, the circulatory lift portion of Eq. (14) is compared with Theodorsen's function [19]. The real portion matches within 2% and the imaginary portion matches within 10%. The relatively small discrepancy can be attributed to the approximation used for the Wagner function.

Experimental data on a pitching wing by Rainey [22] was used for comparison of the total lift response. The total lift response as a function of reduced frequency is plotted in Fig. 15, with Rainey's data marked by circles. The analytical model follows the experimental data trend quite well in both magnitude and phase. As the reduced frequency increases to greater than 0.4, a slight deviation occurs between the experimental data and the total lift response. However, for the experiments presented later in this paper, the reduced frequency remained within the 0.2 to 0.3 range, which matches the Rainey data nicely.

### Wake Effects

Because of the trailed vortex wake system behind any lifting body, the aerodynamic lift on one airfoil segment affects all of the other nine. Consequently, to accurately predict the behavior of the segmented free wing, it was necessary to add downwash effects to the system so that the effective angle of attack on each segment, including the influence of all the others, could be accurately modeled. To model the downwash, the vortex-lattice method [23] was used to calculate an effective angle of attack on each segment, which could then be used to determine the overall lift.

Each wing segment was modeled using a set of horseshoe vortices that consisted of a bound vortex along the quarter-chord of the wing segment and two semi-infinite trailed vortices extending from the ends of the bound segment to infinity aft of the wing. Each segment had a control point placed at the three-quarter-chord centered between the two trailed vortices, as illustrated in Fig. 16.

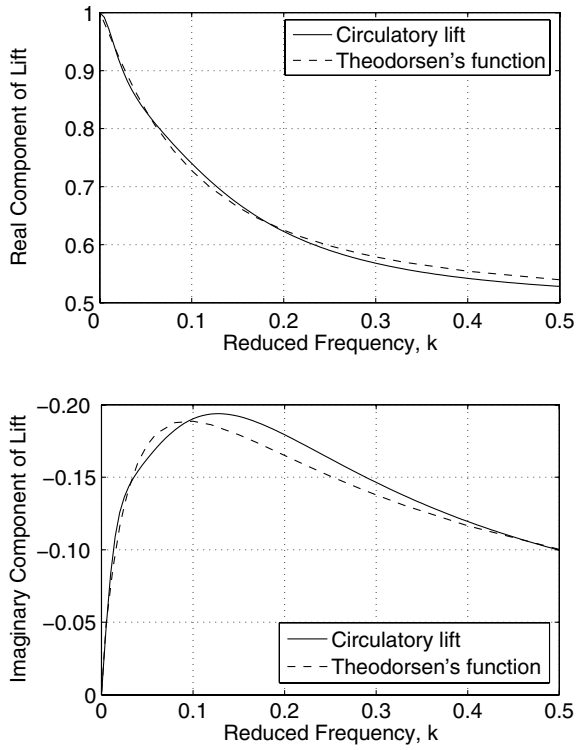


**Fig. 14 Comparison of the analytical model circulatory lift to Theodorsen's function.**

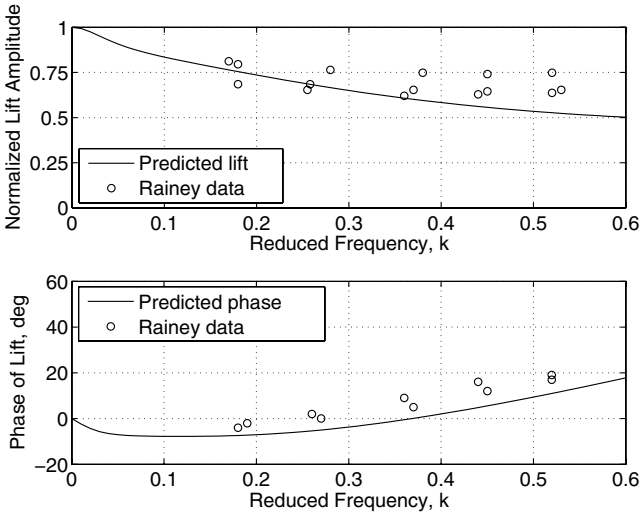


**Fig. 15 Comparison of the analytical model total lift response with pitching data from Rainey [22].**

A boundary condition must be applied in order to compute the strength of the vortices where the "surface of the wing is a streamline" [23]. Since the surface behaves as a streamline, the flow does not pass through the surface of the wing but remains tangent to the surface. For wings with a modest slope of the mean camber line, the tangency condition can be approximated by [23]

$$w_m - v_m \tan\phi + U_\infty\left[\alpha - \left(\frac{\mathrm{d}z}{\mathrm{d}x}\right)_m\right] = 0 \tag{15}$$

For airfoils of modest thickness, a two-dimensional planar approximation for small angles of attack can be used to simplify the tangency condition to

$$w_m = -U_\infty \alpha \tag{16}$$

The downwash at control point $i$ from segment $j$ can be calculated and summed across all segments to get the total downwash $w_{m_i}$,

$$w_{m_i} = \frac{1}{4\pi}\sum_j C_{ij}\Gamma_j \tag{17}$$

as derived by Bertin and Smith [23]. Equating this to Eq. (16) gives a set of equations for the vortex strengths:

$$\frac{1}{4\pi}\sum_j \mathbf{C}_{ij}\Gamma_j = -U_\infty \alpha \tag{18}$$

From the Kutta–Joukowski theorem [16] and the definition of the lift coefficient,

$$L' = \rho U\Gamma = \tfrac{1}{2}\rho U^2 2bC_L \tag{19}$$

Solving for $C_L$ and substituting for $\Gamma$,

$$C_L = \frac{-4\pi}{b}\mathbf{C}^{-1}\alpha = C_{l_\alpha}\alpha_e \tag{20}$$

Finally, solving for $\alpha_e$,

$$\alpha_e = \frac{-4\pi}{bC_{l_\alpha}}\mathbf{C}^{-1}\alpha \tag{21}$$

This matrix equation provides a relationship between the angle of incidence $\alpha$ of each segment and the aerodynamic angle of attack of the segments, including the mutual influences of each segment on all the others. This effective angle of attack could then be substituted

into the aerodynamic equations (10) and (13) to arrive at the total lift and moment per unit span on each segment.

#### Equations of Motion

By combining all the derivations from the previous sections, the equations of motion for the full system were formulated. The system was set up in the following format:

$$\mathbf{E}\,\dot{\mathbf{x}} = \mathbf{A}\mathbf{x} \tag{22}$$

The state vector $\mathbf{x}$ was defined as

$$\mathbf{x} = [\,\dot{\theta}_i \quad \theta_i \quad X_{1,i} \quad X_{2,i} \quad \dot{\phi} \quad \phi]^T \quad \text{for} \quad i = 1, \ldots, 10 \tag{23}$$

The superscript $T$ in Eq. (23) denotes the transpose of the matrix. Solving for $\dot{\mathbf{x}}$, the stability of the system could be analyzed by determining the eigenvalues of the matrix $\mathbf{E}^{-1}\mathbf{A}$. This was performed using the MATLAB program and results will be presented in the form of root-locus plots. The eigenvectors of the system matrix were used to determine the different modes of oscillation of the system.

The equations for pitch, roll, $X_1$, and $X_2$ are shown in order in Eqs. (24–26):

Pitch:

$$\begin{aligned}(\pi\rho b^4 x a^2 + \tfrac{1}{8}\pi\rho b^4 x + I_{yy})\ddot{\theta}_i + (-\pi\rho b^3 x a y_i - 2mb\delta_{x_i} y_i)\ddot{\phi} \\ = (\pi\rho b^3 x U(\tfrac{-1}{2} + a) + \tfrac{1}{8}\rho U b^3 x C_{l_\alpha} C_{ij}(1 - 4a^2))\dot{\theta}_i \\ + (\tfrac{1}{4}\rho U^2 b^2 x C_{l_\alpha} C_{ij}(1 + 2a))\theta_i + (\tfrac{1}{2}\rho U^3 b x C_{l_\alpha} A_1 b_1(1 \\ + 2a))X_{1,i} + (\tfrac{1}{2}\rho U^3 b x C_{l_\alpha} A_2 b_2(1 + 2a))X_{2,i} \\ + (\tfrac{1}{4}\rho U b^2 x C_{l_\alpha} y_j C_{ij}(1 + 2a))\dot{\phi}\end{aligned} \tag{24}$$

Roll:

$$\begin{aligned}(\rho x y_i \pi b^3 a + 2m y_i \delta_{x_i} b)\ddot{\theta}_i + (-\rho x y_i^2 \pi b^2 - I_{xx})\ddot{\phi} = (\rho x y_i \pi b^2 U \\ + \tfrac{1}{4}\rho x y_i U C_{l_\alpha} b^2 C_{ij}(1 - 2a))\dot{\theta}_i + (\tfrac{1}{2}\rho x y_i b U^2 C_{l_\alpha} C_{ij})\theta_i \\ + (\rho x y_i U^3 C_{l_\alpha} A_1 b_1)X_{1,i} + (\rho x y_i U^3 C_{l_\alpha} A_2 b_2)X_{2,i} \\ + (C + \tfrac{1}{2}\rho x y_i y_j U C_{l_\alpha} b C_{ij})\dot{\phi} + K\phi\end{aligned} \tag{25}$$

Unsteady aerodynamic states:

$$\begin{aligned}\begin{bmatrix}\dot{X}_{1,i} \\ \dot{X}_{2,i}\end{bmatrix} = \begin{bmatrix}\frac{-U}{b} b_1 & 0 \\ 0 & \frac{-U}{b} b_2\end{bmatrix} + \begin{pmatrix}1 \\ 1\end{pmatrix}\left[\left(\frac{b}{2U} C_{ij}(1 - 2a)\right)\dot{\theta}_i\right. \\ \left. + C_{ij}\theta_i + \left(\frac{y_j}{U} C_{ij}\right)\dot{\phi}\right]\end{aligned} \tag{26}$$

Combining all of these equations produces a set of 42 coupled first-order differential equations: 10 for $\ddot{\theta}$, 10 for $\dot{\theta}$, 10 for $\dot{X}_1$, 10 for $\dot{X}_2$, one for $\ddot{\phi}$, and one for $\dot{\phi}$. The equations for $\dot{\theta}$ and $\dot{\phi}$ are simply $\dot{\theta} = \dot{\theta}$ and $\dot{\phi} = \dot{\phi}$.

## Analytical Results

To study the dynamics of the segmented-free-wing system, an eigenanalysis was performed on the equations of motion derived above. The goals of this analysis were to understand the nature of the instability, to facilitate predicting its onset, and to find methods for eliminating it.

#### System Properties

To analyze the system, the mass properties of the wing and elastic properties of the mount were needed. The mass moments of inertia $I_{xx}$ and $I_{yy}$ were initially estimated based on approximations of the geometry. After the mass moments of inertia were estimated analytically, they were verified experimentally using a bifilar pendulum [24].

**Table 2 Comparison of analytical and experimental moments of inertia**

| Moment of inertia | Experimental, slug-ft$^2$ | Analytical, slug-ft$^2$ | Difference |
|---|---|---|---|
| Pitching | 0.00536 | 0.00157 | 71% |
| Rolling | 5.087 | 3.883 | 24% |

To obtain the estimated rolling moment of inertia $I_{xx}$, the system was modeled as a rectangular parallelepiped with dimensions of 13.3 ft in span, 16 in. chord, and approximately 3 in. thick. The entire system was weighed to obtain its mass and the rolling moment of inertia was calculated using Eq. (27) [25]:

$$I_{xx} = \tfrac{1}{12} m(\text{span}^2 + \text{thickness}^2) \tag{27}$$

For the pitching moment of inertia $I_{yy}$, the airfoil shape was drawn in the AutoCAD 2004 drawing package and the polar area moment of inertia was calculated using the software's measurement tools. Knowing the density and the span of the wing segment, the estimated pitching mass moment of inertia was calculated. In addition to the wing segment, the counterweight extending beyond the leading edge of the wing was treated as a point mass and its moments of inertia was added accordingly:

$$I_{yy} = J_y x \rho_{\text{seg}} + l^2 m_{cw} \tag{28}$$

The bifilar pendulum was then used to experimentally obtain the mass moments of inertia. Table 2 shows the analytical estimates and experimental measurements. The experimental values are higher than the analytical values, especially for the pitching moment of inertia. The experimental measurements did not account for aerodynamic damping [26] and may consequently overestimate the moments of inertia, particularly the rolling moment of inertia, because of the large surface area.

The spring force in the experimental mounting beam was calculated using the angle of twist equation for a beam and solving for the torque [27]:

$$T = \frac{JG}{L_B}\phi \tag{29}$$

where

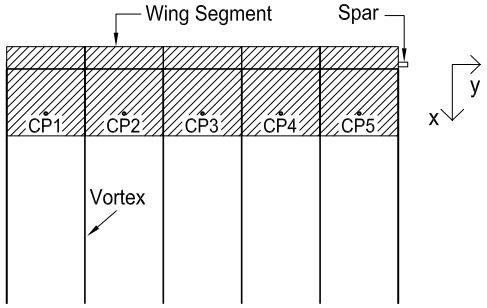


**Fig. 16 Setup of the vortex-lattice method on segmented free wing.**

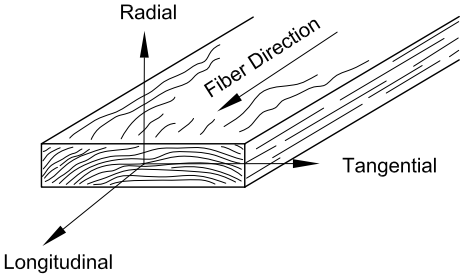


**Fig. 17 Axis orientation for modulus calculations [28].**

**Table 3 Measured spring constant of mounting beam**

| Twist angle, deg | Torque, ft · lb | | | | | | | Average, ft · lb | $K$, ft · lb/rad |
|---|---|---|---|---|---|---|---|---|---|
| 5 | 40 | 45 | 38 | 45 | 45 | 40 | 42 | 42.1 | 482.9 |
| 10 | 80 | 85 | 95 | 80 | —— | —— | —— | 85.0 | 487.0 |
| 15 | 135 | 130 | 125 | 120 | 120 | 120 | —— | 125.0 | 477.5 |

$$K = \frac{JG}{L_B} \tag{30}$$

The mounting beam was fabricated from standard dimensional lumber by laminating two 20-ft-long nominally 2 by 4 in. (1.5 by 3.5 in. actual dimension) pieces of wood stock. The spring force is highly dependent on the species of wood used to make the mounting beam. The spring force varies 400 ft · lb/rad within just a species family. Unfortunately, the exact species of wood was unknown, but it was assumed to be from the pine family. Using the material properties of Lodgepole pine [28], a modulus of rigidity could be calculated for the radial tangential plane of the lumber. A diagram of the axis configuration is shown in Fig. 17. The modulus of rigidity $G$ was calculated to be 964, 800 lb/ft$^2$. This estimated modulus of rigidity was used in the spring constant equation, and an estimated value of $K$ was calculated to be 123.6 ft · lb/rad. No simple analysis for the damping coefficient $C$ was available, so for this initial study the value was assumed to be negligible compared with the aerodynamic forces on the wing system.

To obtain a more accurate value of $K$, the spring force of the beam was experimentally determined by applying a torsional loading to the mounting beam about the longitudinal axis. The spring force was measured by twisting the beam to a predetermined angle and taking a measurement of the applied torque required to achieve the angle using a torque wrench. The beam was twisted to 5, 10, and 15 deg, with several torque readings at each angle to obtain an average. From the torque measurements, $K$ was calculated by dividing the measurement by the respective angle of twist. The experimental results yielded an average $K$ value of 482.5 ft · lb/rad and are shown in Table 3.

#### Eigenanalysis

A root-locus plot of the segmented-free-wing system is shown in Fig. 18. To produce this root-locus plot, the velocity was steadily increased from 1 to 150 ft/s by 0.1 ft/s intervals. The eigenvalues associated with the lowest velocity are denoted by an × and then subsequent eigenvalues are denoted by solid lines. A number of different modes can be identified in the figure. Nine stable pitching modes form a fan shape originating at the origin. These modes represent different motion combinations of the 10 segments in pitch. Some of the mode shapes are not symmetrical left/right, and so they include a small roll component. The differences in the slopes of the root loci for these modes are due to wake effects of each wing segment upon the others. Another set of stable pitching modes are nonoscillatory and thus lie on the real axis.

There are two rolling modes associated with the system. One of the modes is stable. It starts at the origin and increases in frequency and damping as velocity increases. The second mode is the unstable rolling mode that was seen in the experimental testing of the segmented free wing. Because the wing is rigidly attached to the mounting beam, at zero velocity this mode starts as an undamped oscillation at the natural frequency of the beam/wing system. As velocity increases, the mode initially moves into the left/stable half of the plane before moving back to the right and becoming unstable. The oscillation frequency decreases slightly as velocity starts to increase, but then stays roughly constant as the speed continues to increase and the mode becomes unstable. This is more easily seen in Fig. 19, which is a magnified view of the previous root-locus plot, focusing in on this unstable mode.

The analytical model predicts a crossover velocity, the velocity at which the system becomes dynamically unstable, of 49.5 ft/s and an oscillation frequency at that speed of 1.3 Hz. In the experimental results, the velocity at which the segmented free wing became unstable was between 22 and 29 ft/s, and the oscillation frequency was observed to be approximately 1.2 Hz. Thus, the analytical model predicts a significantly more stable system than that observed, though the oscillation frequency is predicted within 10%.

The source of the discrepancy between the observed behavior and the analytical results is not completely clear. The experimental test was preliminary and limited instrumentation was used. However, the discrepancy between the experimental result and analytical result is well outside the bounds of experimental uncertainty. Several possible origins of this discrepancy have been considered, including errors in the estimated system properties, inadequate structural or aerodynamic modeling, and attributes of the system that were not modeled. Examples of the system properties that may be inaccurate include the spring constant of the mounting beam, the mass moments of inertia of the wings in pitch and roll, the center-of-gravity position of the airfoil, and the aerodynamic center of the airfoil.

The uncertainty in the spring constant of the mounting beam comes from a limitation in the testing. A torque wrench was attached to the front of the supporting beam. The beam was then torqued until a particular angle of twist was achieved, followed by recording the value from the torque wrench. A problem with this method of measuring the spring constant arises from the downward bending of the beam from the way the torque was applied. The effect of the bending of the beam on the measured torque is unknown. In addition, the accuracy of the torque wrench was not verified.

The pitching and rolling mass moments of inertia were measured via a bifilar pendulum. For both the rolling and pitching mass

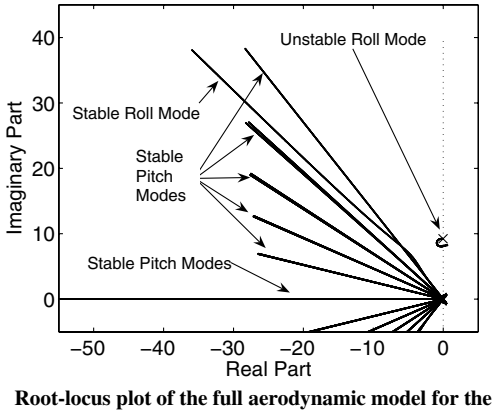


**Fig. 18 Root-locus plot of the full aerodynamic model for the model.**

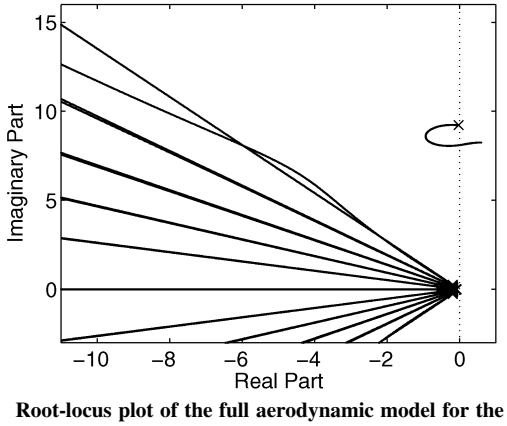


**Fig. 19 Root-locus plot of the full aerodynamic model for the model, magnified.**

moments of inertia, the damping of the displaced volume of air during the bifilar pendulum test was not modeled and was ignored in all calculations of mass moments of inertia. These damping effects were ignored because there is no simple means of estimating or measuring them. The pitching mass moment of inertia was measured for only one segment and was assumed to apply for all of the segments of the segmented free wing. The quantity of internal wires and their position, the counterweight mass and position, and variable segment mass all contribute to an uncertainty in the pitching mass moment of inertia.

The location of the center of gravity of each individual segment varies in each segment, depending on the location of the control surface wires that run laterally through the internal spaces of the airfoil aft of the spar. The segments were balanced as accurately as possible, but during testing the wires were free to move and could shift the center of gravity of the segment a finite amount, depending on the number of control wires running through the individual wing segment.

The aerodynamic center of the wing sections was estimated using the Xfoil software package. Although this software is well regarded and has been used for quite a number of design and analysis studies [17,18], there is some uncertainty associate with its estimate. Moreover, variations in the surface of each wing segment could affect the location of the aerodynamic center. An Xfoil analysis of the airfoil with and without forced transition of the boundary layer indicated that forcing transition of the boundary layer from laminar to turbulent would shift the aerodynamic center about 0.5% of the chord. The free-wing segments tested were covered with a plastic laminate, and small wrinkles and ridges were present on the surface from the laminate, which could easily affect boundary-layer transition. Consequently, it is likely that there would be variations in the aerodynamic center position from one segment to another.

### Aerodynamic Model Sensitivities

The potential errors in the input parameters of the system mentioned in the previous section could have a large effect on the analytical model's prediction of when the system will become unstable, measured by the crossover velocity. To better understand the analytical model's sensitivities to these parameters, a study was performed by slightly changing the input values and observing the change in the crossover velocity. The parameters examined were the rolling moment of inertia, pitching moment of inertia, aerodynamic center, center-of-gravity position, and the spring constant. Each value was varied to show the behavior in the general vicinity of the predicted value. The spring force and mass moments of inertia were varied by $\pm 25\%$and $\pm 50\%$, and the aerodynamic center was varied between 27 and 31% of the chord. The center-of-gravity position was varied from 5% aft of the spar to 3% forward of the spar.

Figure 20 shows the variation of crossover velocity and frequency at crossover as a function of pitching mass moment of inertia. Increasing the pitching mass moment of inertia decreases both the crossover velocity and the crossover frequency. The change in frequency is quite small when compared with the change in velocity associated with the increase in pitching mass moment of inertia. However, as the moment of inertia continually increases, the frequency falloff rate increases. The change in crossover velocity is more extreme in the lower regions of the pitching mass moment of inertia and begins to level off as it increases to 0.008 slugs-ft$^2$.

Changes in the rolling mass moment of inertia are similar to that of the pitching mass moment of inertia. Unlike the crossover frequency associated with the pitching mass moment of inertia, the rate of change of the crossover frequency decreases as the rolling moment of inertia is increased. The crossover frequency for the changing rolling mass moment of inertia follows the same behavior as the crossover velocity. As the rolling mass moment of inertia is increased, the system becomes increasingly unstable and the crossover velocity is decreased, as shown in Fig. 21.

Shifting the aerodynamic center of the airfoil, as shown in Fig. 22, produces a similar result for the crossover velocity when compared with changes in the mass moments of inertia. The crossover

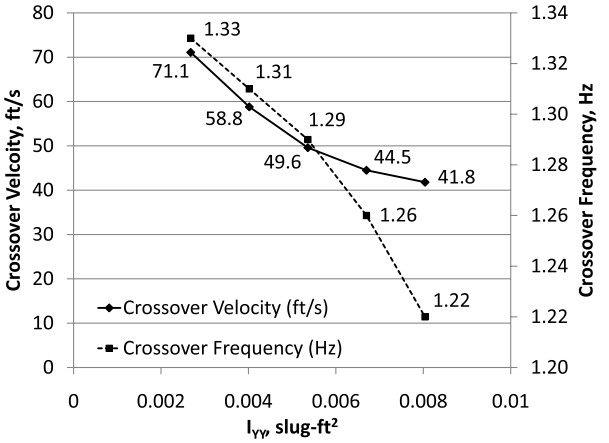


**Fig. 20 Full aerodynamic model sensitivity to changes in pitching mass moment of inertia.**

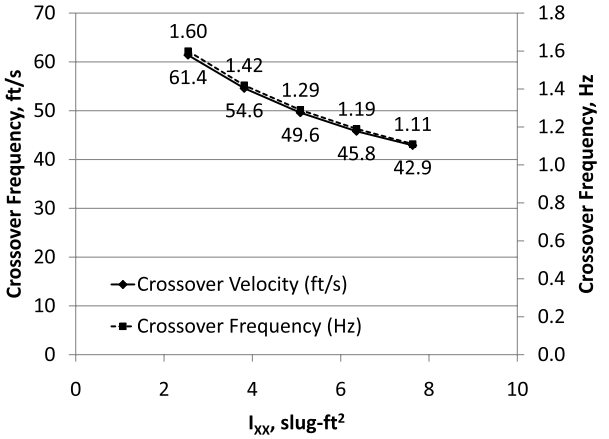


**Fig. 21 Full aerodynamic model sensitivity to changes in rolling mass moment of inertia.**

frequency, however, behaves in a much different manner. As the aerodynamic center is moved aft, the crossover frequency increases almost linearly. As mentioned previously, the crossover velocity follows the same trend as the mass moments of inertia, in that the changes in velocity are greater when the aerodynamic center is forward.

Changes in the center-of-gravity position of each wing segment from the hinge location (Fig. 23) causes a linear change in both the crossover velocity and frequency. The crossover frequency decreases linearly as the hinge location is moved forward from behind the hinge location to ahead of the hinge location. In contrast to the crossover

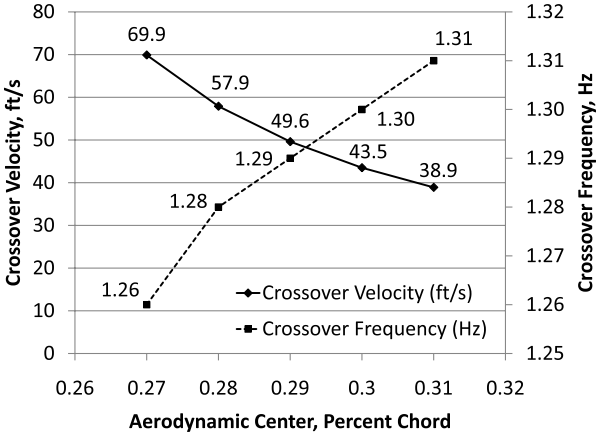


**Fig. 22 Full aerodynamic model sensitivity to changes in the aerodynamic center.**

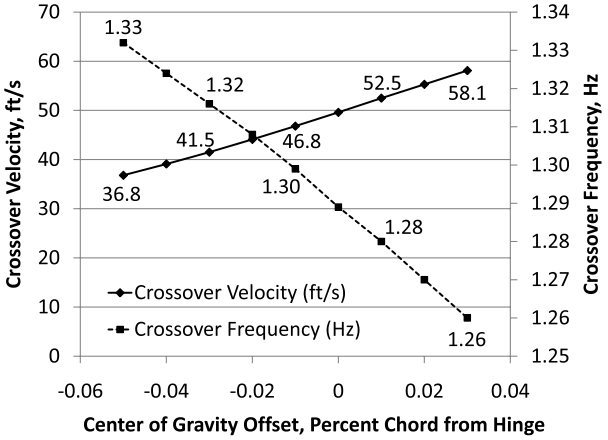


**Fig. 23 Full aerodynamic model sensitivity to changes in the center-of-gravity position.**

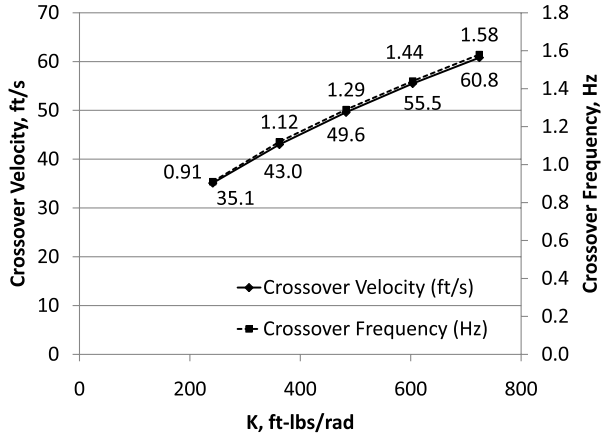


**Fig. 24 Full aerodynamic model sensitivity to changes in the spring constant *K*.**

frequency, the crossover velocity decreases as the center-of-gravity position moves aft. It is believed from experience in the experimental trials that the center-of-gravity position is aft of the hinge location, due to a shift in the position of the internal control wires during flight. The wires were housed in a chamber that allowed the wires to vary in position from 4.125 to 6.25 in. aft of the leading edge of the segment. If the wing segments were perfectly balanced with the wires in the most forward position, the center of gravity would shift aft during flight as the wires shifted aft. This would produce a segment imbalance and a center-of-gravity offset of approximately 2%. If the center-of-gravity position was shifted 2% aft of the hinge location, the predicted crossover velocity changed to 44.1 ft/s.

The spring constant was also varied to show the full aerodynamic model's sensitivity. Figure 24 shows how the crossover velocity and frequency changes as the spring constant is both increased and decreased. Both the crossover velocity and frequency follow the same trend and increase as $K$ is increased.

### Variation of Input Parameters Based Upon Error Estimates

As demonstrated in the previous section, model parameters strongly affect the predicted crossover velocity and frequency produced by the analytical model. To determine the effect of multiple simultaneous changes in input parameters, an analytical test was performed by adjusting each of the parameters at the same time. Each parameter was adjusted by estimating the most likely error in that parameter.

**Table 4 Baseline and trial parameter values**

| Parameter | Baseline value | Trial value |
|---|---|---|
| $I_{xx}$ | 5.087 slug-ft$^2$ | 4.070 slug-ft$^2$ |
| $I_{yy}$ | 0.00536 slug-ft$^2$ | 0.00482 slug-ft$^2$ |
| $\delta_x$ | 0% | 4% chord aft of hinge |
| $x_{ac}$ | 29% | 31% |
| $K$ | 482.5 ft · lb/rad | 337.75 ft · lb/rad |

The measured mass moments of inertia were assumed to be overestimates, due to the ignored damping of the displaced air around the model when spinning on the bifilar pendulum. It is estimated that the damping effect is greater in the rolling moment of inertia than the pitching moment of inertia, due to the larger surface area perpendicular to the movement. Consequently, the rolling mass moment of inertia was reduced by 20% and the pitching mass moment of inertia was reduced by 10%.

Balancing each individual wing segment was difficult due to the variability in the internal wire positions. Because of the difficulty in balancing the segments and the wires' ability to move inside the segments, the center of gravity of each individual segment was most likely not centered on the hinge, but rather aft of the hinge. For this trial, the center-of-gravity position was shifted aft to 4% of the chord behind the hinge location.

The Xfoil analysis of the aerodynamic center showed that early transition of the boundary layer from laminar to turbulent would shift the aerodynamic center aft. With free transition, the predicted aerodynamic center was 29% of the chord. An aft shift to 31% was assumed for this trial.

The initial analytical estimate of the wood beam spring constant was approximately 125 ft · lb/rad. The measured value was 482.5 ft · lb/rad. Because the measured value was considerably higher than the estimate, for this trial the measured value was assumed to be an overestimate and a 30% reduction was applied.

The analytical model was run with these new trial values , which are summarized in Table 4. Figure 25 shows the root-locus plot for the model with the trial parameter values, and Fig. 26 shows the same plot magnified to highlight the unstable mode. Qualitatively, the results look very similar to those shown before (e.g. Fig. 18) with the baseline parameters. However, with the new parameters, the crossover velocity decreased to 29.9 ft/s and the crossover frequency is 1.23 Hz. These results match the experimental results closely. This indicates that errors in the measured/estimated system parameters could explain much of the discrepancy between the analytical results and the experimental results.

### Analysis with Fixed Segments

The analytical model was also used to examine the segmented free wing with fixed segments added to the wingtips. During experimental testing, all the fixed segments were successful at stabilizing the system up to the maximum speed tested. The same conditions were examined using the analytical model. For all of the fixed segment widths (6, 12, 18, and 24 in.), the analytical model predicted a stable system up to the 150 ft/s maximum speed examined. An example root-locus plot is presented in Fig. 27 for the 6 in. fixed segment width and it shows the now stable rolling mode becoming

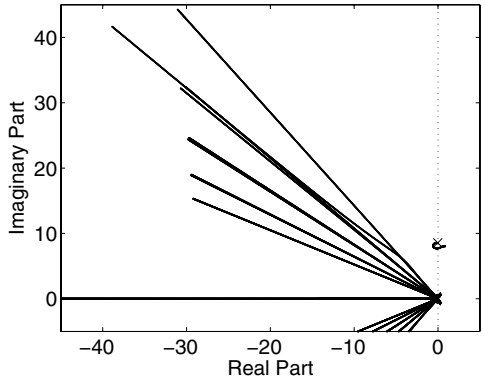


**Fig. 25 Root-locus plot of the full aerodynamic model with modified input parameters.**

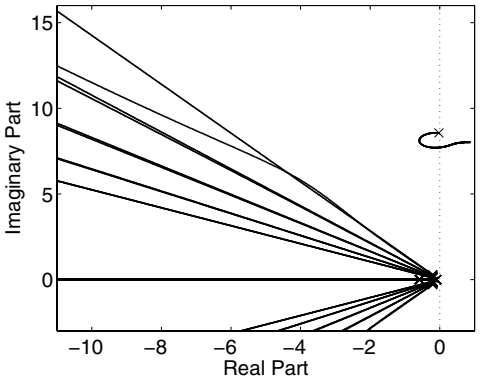


**Fig. 26 Root-locus plot of the full aerodynamic model with modified input parameters, magnified to reveal unstable roots.**

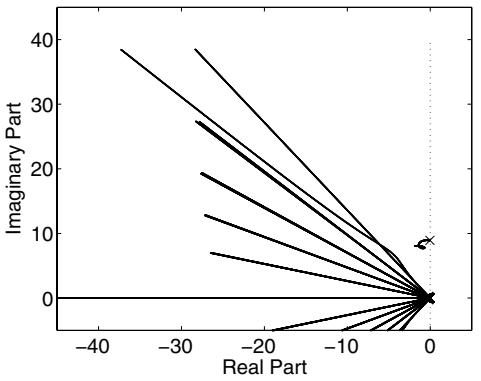


**Fig. 27 Root-locus plot for the full aerodynamic model for the system with fixed segments.**

increasing stable as velocity increases. All the modes from the previous root-locus plot of the same system setup are present and exhibit the same behavior (compare with Fig. 18).

Zooming into the origin, the behavior of the newly stable rolling mode can easily be seen in the upper right of Fig. 28. The mode starts left and turns back to the right as it did previously, but now instead of continuing to the right and becoming unstable, it reverses and moves left again. Also, as the velocity is increased the oscillation frequency remains almost constant. Similar behavior is observed with larger segments; however, the size of the loop formed increases and moves to the left indicating an increase in the damping for that mode.

These analytical results in conjunction with the experimental results on the larger model with the fixed segments indicate that a small fixed segment at the tip of each wing panel is sufficient to stabilize the system and avoid the dynamic instability. The analytical

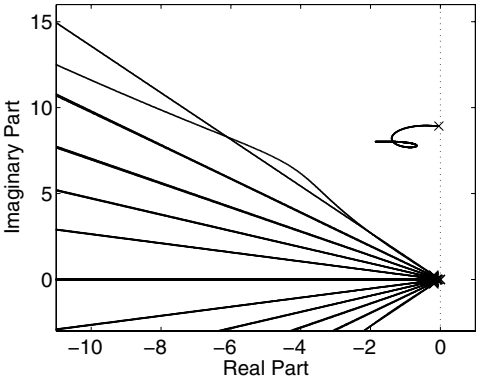


**Fig. 28 Root-locus plot for the full aerodynamic model for the system with fixed segments attached, magnified about the origin.**

model indicated that a fixed segment as small as 2 in. wide would be sufficient to stabilize the system.

## Conclusions

A wind-tunnel model of the segmented free wing was constructed and tested in the Auburn University wind tunnel. Initial results from a wind-tunnel test showed a 38% reduction in the rolling moment response to spanwise flow variations when compared with a conventional free wing. These positive results showed that the segmented free wing does have the capability to respond to both time-varying and span-varying turbulence.

After the initial testing of the wind-tunnel model, a 13.3-ft-span model of a segmented free wing was designed and fabricated. Initial aerodynamic testing was conducted by mounting this wing on a rig attached to a pickup truck. A repeatable divergent rolling oscillation emerged at velocities as low as 22 to 29 ft/s. From previous results published by Porter and Brown [10], the divergent mode was presumed to be related to the divergent spiral mode associated with free wings when the left and right wings are allowed to be torsionally independent of each other.

Several modifications to the segmented-free-wing properties were made in attempts to stabilize the system and included changing the rolling mass moment of inertia, the center-of-gravity position, and the number of segments. None of the modifications to the properties increased the stability of the segmented free wing. The crossover velocity at which the wings began to oscillate was virtually unchanged and significant changes in the frequency of the oscillation were not seen.

The segmented-free-wing design was modified by adding fixed segments to the wing tips varying in size from 6 to 24 in. in span. All the fixed segments provided dynamic stability to the system for all experimental velocities.

An analytical model was developed in response to the experimental testing of the segmented free wing. The computer model, using eigenanalysis, was successfully able to predict the divergent oscillation. The velocity at which the analytical model predicted the oscillation to occur was higher than that in experimentation. Errors in the model parameters used in the model may have contributed to this discrepancy. When the parameters were modified based upon estimates of the error, the same divergent modes were predicted, but the crossover velocity at which the oscillation occurred dropped to 29.9 ft/s, which is within the upper bound of the experimental velocity. When the fixed segments were attached in the analytical model, the results matched the experimental results: the oscillation was damped out and the system was dynamically stable.

Overall, the segmented-free-wing concept is intended for use in adverse environments in which span-varying conditions are a significant problem. Initial test results indicate that significant reductions in structural moments induced by both span-varying and time-varying gust fields are possible. It is anticipated that this concept will be most applicable to aircraft with low wing loadings and large wing spans such as high-altitude, long-endurance unmanned aircraft. For such aircraft, the segmented-free-wing design could significantly reduce the structural loads encountered by the aircraft when subjected to turbulence and gust fields. By reducing these structural loads, the structural weight fraction of the aircraft may be able to be reduced, providing an increase in useful load and in the overall utility of the design.

## Acknowledgments

The authors would like to thank Robert Gross for allowing the use of his truck for the experimental testing and Anwar Ahmed for the use of the wind tunnel. The authors would also like to acknowledge Andy Weldon for his help in fabricating parts for both the wind-tunnel model and the large-scale model. The authors would like to thank Brian C. Reitz for his help with the electronics on the large-scale model and working with the radio-controlled transmitter. Finally, the authors would like to thank Neal Allgood for his help in the fabrication of the experimental model and Kevin Albarado for his help in the wind tunnel.

## References


[1] Noll, T. E., "Investigation of the Helios Prototype Aircraft Mishap," NASA Langley Research Center, Jan. 2004, http://www.nasa.gov/pdf/64317main_helios.pdf [retrieved 22 Feb. 2009].

[2] Croft, J., "Airbus and Boeing Spar for Middleweight Title," *Aerospace America*, July 2005, pp. 36–42.

[3] Scherz, C. J., and Tucker, P. B., "Flight Test Evaluation of Active Ride Control System for Tactical Aircraft," AIAA Guidance, Navigation, and Control Conference, Snowmass, CO, AIAA Paper 1985-1860, Aug. 1985.

[4] Hess, R. A., "Optimal Stochastic Control and Aircraft Gust Alleviation," *Journal of Aircraft*, Vol. 8, No. 4, April 1971, pp. 284–286. doi:10.2514/3.44273

[5] Cox, C., Gopalarathnam, A., and Hall, C. E., "Development of Stable Automated Cruise Flap for an Aircraft with Adaptive Wing," *Journal of Aircraft*, Vol. 46, No. 1, Jan.–Feb. 2009, pp. 301–311. doi:10.2514/1.38684

[6] Etkin, B., "Turbulent Wing and Its Effect on Flight," *Journal of Aircraft*, Vol. 18, No. 5, May 1981, pp. 327–345. doi:10.2514/3.57498

[7] Roesch, P., and Harlan, R. B., "A Passive Gust Alleviation System for Light Aircraft," AIAA Mechanics and Control of Flight Conference, Anaheim, CA, AIAA Paper 1974-773, Aug. 1974.

[8] Miller, S., Vio, G. A., Cooper, J. E., and Sensburg, O., "Optimisation of a Scaled Sensorcraft MOdel with Passive Gust Alleviation," AIAA/ISSMO Multidisciplinary Analysis and Optimization Conference, AIAA Paper 2008-5875, Victoria, BC, Canada, Sept. 2008.

[9] Vio, G. A., and Cooper, J. E., "Optimisation of the Composite Sensorcraft Structure for Gust Alleviation," AIAA/ISSMO Multidisciplinary Analysis and Optimization Conference, AIAA Paper 2008-6017, Victoria, BC, Canada, Sept. 2008.

[10] Porter, R. F., and Brown, J. H., Jr., "Evaluation of the Gust-Alleviation Characteristics and Handling Qualities of a Free-Wing Aircraft," NASA CR-1523, Apr. 1970.

[11] Porter, R. F., Luce, R. G., and Brown, J. H., Jr., "Investigation of the Applicability of the Free-Wing Principle to Light, General Aviation Aircraft," NASA CR-2046, June 1972.

[12] Porter, R. F., Hall, D. W., Brown, J. H., Jr., and Gregorek, G. M., "Analytical Study of a Free-Wing/Free-Trimmer Concept," NASA 2378, Feb. 1978.

[13] Porter, R. F., Hall, D. W., and Vergara, R. D., "Extended Analytical Study of the Free-Wing/Free-Trimmer Concept," NASA CR-3135, April 1979.

[14] Sandlin, D. R., "Wind Tunnel Test of a Free-Wing/Free-Trimmer Model," NASA CR-170394, Dec. 1982.

[15] Recktenwald, B. D., *Aerodynamic Testing of a Circular Planform Concept Aircraft*, M.S. Thesis, Auburn Univ., Auburn, AL, May 2008.

[16] Anderson, J. D., Jr., *Fundamentals of Aerodynamics*, 4th ed., McGraw–Hill, New York, 2007.

[17] Drela, M., and Giles, M. B., "Viscous-Inviscid Analysis of Transonic and Low Reynolds Number Airfoils," *AIAA Journal*, Vol. 25, No. 10, Oct. 1987, pp. 1347–1355. doi:10.2514/3.9789

[18] Drela, M., "XFOIL: An Analysis and Design System for Low Reynolds Number Airfoils," *Low Reynolds Number Aerodynamics*, edited by T. J. Mueller, Lecture Notes in Engineering, Vol. 54, Springer–Verlag, New York, 1989.

[19] Fung, Y. C., *An Introduction to the Theory of Aeroelasticity*, Galcit Aeronautical Series, Wiley, New York, 1955.

[20] Jones, R. T., *The Unsteady Lift of a Wing of Finite Aspect Ratio*, NACA Rept. 681, 15 June 1939.

[21] Johnson, W., *Helicopter Theory*, Dover, New York, 1994.

[22] Rainey, A. G., "Measurement of Aerodynamic Forces for Various Mean Angles of Attack on an Airfoil Oscillating in Pitch and on Two Finite-Span Wings Oscillating in Bending with Emphasis on Damping in the Stall," NACA TR-1305, 1957.

[23] Bertin, J. J., Jr., and Smith, M. L., *Aerodynamics for Engineers*, 1st ed., Prentice–Hall, Upper Saddle River, NJ, 1979.

[24] Welstead, J., *Stability Analysis of a Segmented Free-wing Concept for UAS Gust Alleviation in Adverse Environments*, M.S. Thesis, Auburn Univ., Auburn, AL, Aug. 2009.

[25] Ginsberg, J., *Engineering Dynamics*, 1st ed., Cambridge Univ. Press, New York, 2008.

[26] Then, J. W., and Chiang, K. B., "Experimental Determination of Moments of Inertia by the Bilar Pendulum Method," *American Journal of Physics*, Vol. 38, No. 4, April 1970, pp. 537–539. doi:10.1119/1.1976385

[27] Hibbeler, R. C., *Statics and Mechanics of Materials*, 2nd ed., Pearson Prentice Hall, Upper Saddle River, NJ, 2008.

[28] Wood Handbook—Wood as an Engineering Material, Forest Products Lab., U.S. Dept. of Agriculture, Madison, WI, 1999.